Coupling of a crystal plasticity finite-element model with a probabilistic cellular automaton for simulating primary static recrystallization in aluminium

Dierk Raabe† and Richard C Becker‡

† Max-Planck-Institut für Eisenforschung, Max-Planck-Str. 1, 40237 Düsseldorf, Germany
‡ Lawrence Livermore National Laboratory, 7000 East Avenue, L-170 Livermore, CA 94550, USA

Abstract. The paper presents a two-dimensional approach for simulating primary static recrystallization, which is based on coupling a viscoplastic crystal plasticity finite-element model with a probabilistic kinetic cellular automaton. The crystal plasticity finite-element model accounts for crystallographic slip and for the rotation of the crystal lattice during plastic deformation. The model uses space and time as independent variables and the crystal orientation and the accumulated slip as dependent variables. The ambiguity in the selection of the active slip systems is avoided by using a viscoplastic formulation that assumes that the slip rate on a slip system is related to the resolved shear stress through a power-law relation. The equations are cast in an updated Lagrangian framework. The model has been implemented as a user subroutine in the commercial finite-element code Abaqus. The cellular automaton uses a switching rule that is formulated as a probabilistic analogue of the linearized symmetric Turnbull kinetic equation for the motion of sharp grain boundaries. The actual decision about a switching event is made using a simple sampling nonMetropolis Monte Carlo step. The automaton uses space and time as independent variables and the crystal orientation and a stored energy measure as dependent variables. The kinetics produced by the switching algorithm are scaled through the mesh size, the grain boundary mobility, and the driving force data. The coupling of the two models is realized by: translating the state variables used in the finite-element plasticity model into state variables used in the cellular automaton; mapping the finite-element integration point locations on the quadratic cellular automaton mesh; using the resulting cell size, maximum driving force, and maximum grain boundary mobility occurring in the region for determining the length scale, time step, and local switching probabilities in the automaton; and identifying an appropriate nucleation criterion. The coupling method is applied to the two-dimensional simulation of texture and microstructure evolution in a heterogeneously deformed, high-purity aluminium polycrystal during static primary recrystallization, considering local grain boundary mobilities and driving forces.

1. Motivation for coupling different spatially discrete microstructure and texture simulation methods

Time- and space-discretized simulation approaches such as the crystal plasticity finite-element method or cellular automata are increasingly gaining momentum as powerful tools for predicting microstructures and textures. The major advantage of such discrete methods is that they consider material heterogeneity as opposed to classical statistical approaches, which are based on the assumption of material homogeneity.

Although the average behaviour of materials during deformation and heat treatment can sometimes be sufficiently well described without considering local effects, prominent

examples exist where substantial progress in understanding and tailoring material response can only be attained by taking material heterogeneity into account. For instance, in the field of plasticity the quantitative investigation of ridging and roping, or related surface defects observed in sheet metals, requires knowledge about local effects such as the grain topology or the form and location of second phases. In the field of heat treatment, the origin of the Goss texture in transformer steels, the incipient stages of cube texture formation during primary recrystallization of aluminium, the reduction of the grain size in microalloyed low-carbon steel sheets, and the development of strong $\{111\}\langle uvw \rangle$ textures in steels can hardly be predicted without incorporating local effects such as the orientation and location of recrystallization nuclei and the character and properties of the grain boundaries surrounding them.

Although spatially discrete microstructure simulations have already profoundly enhanced our understanding of microstructure and texture evolution over the last decade, their potential is sometimes simply limited by an insufficient knowledge about the external boundary conditions that characterize the process and an insufficient knowledge about the internal starting conditions that are, to a large extent, inherited from the preceding process step. It is thus an important goal to improve the incorporation of both types of information into such simulations. External boundary conditions prescribed by real industrial processes are often spatially nonhomogeneous. They can be investigated using experiments or process simulations that consider spatial resolution. Spatial heterogeneities in the internal starting conditions, i.e. in the microstructure and texture, can be obtained from experiments or microstructure simulations that include spatial resolution.

In this paper we use the results obtained from a crystal plasticity finite-element simulation as starting conditions for a discrete recrystallization simulation carried out with a probabilistic cellular automaton. The coupling between both methods consists of: extracting and translating the state variables of the finite-element plasticity model (texture and accumulated shear) into state variables of the cellular automaton model (texture and dislocation density); mapping these data on the cellular automaton grid; scaling the cellular automaton mesh in terms of the derived cell size, maximum occurring driving force and grain boundary mobility; and in establishing an adequate nucleation criterion which makes use of these data.

The plan of the paper is as follows: we will separately present the basic features of both simulation methods in sections 2 and 3, explain the coupling method in section 4, and present the results of the recrystallization simulations in section 5.

2. The crystal plasticity finite-element model

2.1. Crystal constitutive model

The deformation behaviour of the grains is determined by a crystal plasticity model, which accounts for plastic deformation by crystallographic slip and for the rotation of the crystal lattice during deformation. Consequently, the model uses space and time as independent variables and the crystal orientation and the accumulated slip as dependent or state variables†. The crystal kinematics follow those described by Asaro (1983), and the rate-dependent formulation follows that developed by Peirce *et al* (1983). Here, however, the equations are cast in an updated Lagrangian framework rather than the total Lagrangian. The model has been implemented (Smelser and Becker 1989) as a user subroutine in the commercial finite-element code Abaqus and has been used in several studies to simulate deformation in grains and single crystals (Becker 1991, Becker *et al* 1991, 1995).

---

† The accumulated slip can be regarded as a state variable since it is used for the calculation of the slip system's resistance to shear.

In the crystal model, the velocity gradient, $\boldsymbol{L}$, is decomposed additively into elastic and plastic parts:

$$\boldsymbol{L} = \boldsymbol{L}^* + \boldsymbol{L}^{\mathrm{p}}. \tag{1}$$

Each of these can be further decomposed into its symmetric and antisymmetric parts representing, respectively, the rate of deformation tensor, $\boldsymbol{D}$, and the spin tensor, $\boldsymbol{\Omega}$:

$$\boldsymbol{L}^* = \boldsymbol{D}^* + \boldsymbol{\Omega}^* \tag{2}$$

$$\boldsymbol{L}^{\mathrm{p}} = \boldsymbol{D}^{\mathrm{p}} + \boldsymbol{\Omega}^{\mathrm{p}}. \tag{3}$$

The plastic part of the rate of deformation tensor, $\boldsymbol{D}^{\mathrm{p}}$, and the plastic spin, $\boldsymbol{\Omega}^{\mathrm{p}}$, can be expressed in terms of the slip rates, $\dot{\gamma}^\alpha$, along the crystallographic slip directions $\boldsymbol{s}_\alpha$ and on crystallographic slip planes with normals $\boldsymbol{m}_\alpha$:

$$\boldsymbol{D}^{\mathrm{p}} = \frac{1}{2} \sum_{\alpha=1}^{N} \dot{\gamma}^\alpha (\boldsymbol{s}_\alpha \otimes \boldsymbol{m}_\alpha + \boldsymbol{m}_\alpha \otimes \boldsymbol{s}_\alpha) = \sum_{\alpha=1}^{N} \dot{\gamma}^\alpha \boldsymbol{P}_\alpha \tag{4}$$

$$\boldsymbol{\Omega}^{\mathrm{p}} = \frac{1}{2} \sum_{\alpha=1}^{N} \dot{\gamma}^\alpha (\boldsymbol{s}_\alpha \otimes \boldsymbol{m}_\alpha - \boldsymbol{m}_\alpha \otimes \boldsymbol{s}_\alpha) = \sum_{\alpha=1}^{N} \dot{\gamma}^\alpha \boldsymbol{W}_\alpha \tag{5}$$

where $\boldsymbol{s}_\alpha \otimes \boldsymbol{m}_\alpha$ and $\boldsymbol{m}_\alpha \otimes \boldsymbol{s}_\alpha$ are the dyadic products of the slip vectors.

For the simulations on aluminium, which has a face-centred cubic (fcc) crystal structure, plastic deformation at low temperatures is typically assumed to occur on the 12 slip systems with $\langle 110 \rangle$ slip directions and $\{111\}$ slip planes, i.e. the slip vectors $\boldsymbol{s}_\alpha = \frac{1}{\sqrt{2}}(110)^{\mathrm{T}}$ and $\boldsymbol{m}_\alpha = \frac{1}{\sqrt{3}}(111)^{\mathrm{T}}$ are orthonormal.

The elastic stretch and the elastic rotation of the crystal lattice lead to a change of $\boldsymbol{s}_\alpha$ and $\boldsymbol{m}_\alpha$. This effect is captured by the elastic part of the velocity gradient. The slip vectors evolve during deformation according to

$$\dot{\boldsymbol{s}}_\alpha = \boldsymbol{L}^* \cdot \boldsymbol{s}_\alpha \tag{6}$$

$$\dot{\boldsymbol{m}}_\alpha = -\boldsymbol{m}_\alpha \cdot \boldsymbol{L}^*. \tag{7}$$

The slip vectors remain orthogonal so that the plastic portion of the deformation is nondilatant. By assuming a stress potential in which the stress is related to the elastic distortion of the crystal lattice, the rate of the Kirchhoff stress tensor, $\dot{\boldsymbol{\tau}}$, is given by

$$\dot{\boldsymbol{\tau}} = \mathbf{C} : \boldsymbol{D}^* + \boldsymbol{D}^* \cdot \boldsymbol{\tau} + \boldsymbol{\tau} \cdot \boldsymbol{D}^* + \boldsymbol{\Omega}^* \cdot \boldsymbol{\tau} - \boldsymbol{\tau} \cdot \boldsymbol{\Omega}^* \tag{8}$$

where $\mathbf{C}$ is a fourth-order tensor of the elastic moduli and $\boldsymbol{\tau}$ is the Kirchhoff stress tensor. Using the additive decomposition of the rate of deformation tensor and the spin into its elastic and plastic portions, and combining the second and third terms of equation (8) with the modulus to define a new fourth-order tensor, $\mathbf{K}$, the Jaumann rate tensor of the Kirchhoff stress rate can be written

$$\overset{\triangledown}{\boldsymbol{\tau}} = \mathbf{K} : \boldsymbol{D}^* - \mathbf{K} : \boldsymbol{D}^{\mathrm{p}} - \boldsymbol{\Omega}^{\mathrm{p}} \cdot \boldsymbol{\tau} + \boldsymbol{\tau} \cdot \boldsymbol{\Omega}^{\mathrm{p}} = \mathbf{K} : \boldsymbol{D}^* - \sum_{\alpha=1}^{N} \dot{\gamma}^\alpha \boldsymbol{R}_\alpha. \tag{9}$$

The last three terms of equation (9) involve plastic deformation. They can be expressed in terms of slip rates as

$$\sum_{\alpha=1}^{N} \dot{\gamma}^\alpha (\mathbf{K} : \boldsymbol{P}_\alpha + \boldsymbol{W}_\alpha \cdot \boldsymbol{\tau} - \boldsymbol{\tau} \cdot \boldsymbol{W}_\alpha) = \sum_{\alpha=1}^{N} \dot{\gamma}^\alpha \boldsymbol{R}_\alpha \tag{10}$$

where P_α and W_α are defined in equations (4) and (5). Using equation (10), the Jaumann stress rate is given by

$$\overset{\triangledown}{\tau} = \mathbf{K} : D^* - \sum_{\alpha=1}^{N} \dot{\gamma}^\alpha R_\alpha. \tag{11}$$

The fourth-order modulus tensor, $\mathbf{K}$, is given in terms of the crystal moduli and the current stress state. The tensors R_α are functions of the stress state and of the known crystal geometry.

What remains is to specify the slip rates, $\dot{\gamma}^\alpha$. In the rate-dependent constitutive formulation adopted here, the slip rate on a slip system is assumed to be related to the resolved shear stress on this system, $\tau^\alpha = \tau : P_\alpha$, through a power law relation:

$$\dot{\gamma}^\alpha = \dot{\gamma}_0^\alpha \left(\frac{\tau^\alpha}{\hat{\tau}^\alpha} \right)^{1/m} \tag{12}$$

where the scalar scaling parameter $\hat{\tau}^\alpha$, which has the unit of stress, is a phenomenological measure for the slip system strength or resistance to shear, $m = 0.002$ is the strain rate sensitivity exponent, and $\dot{\gamma}_0^\alpha = 0.03 \text{ s}^{-1}$ is a reference shear rate. The value of the strain rate sensitivity exponent is low and the material response is almost rate-independent.

With the slip rates given as explicit functions of the known resolved shear stresses, the rate-dependent method avoids the ambiguity in the selection of active slip systems, which is encountered in many rate-independent formulations where it must be solved using an additional selection criterion. However, integration of the stress rate, equation (11), with the slip rate defined by equation (12) produces a system of equations which is numerically 'stiff'. The rate tangent modulus method of Peirce *et al* (1983) is used to increase the stable time step size.

For the present simulations, the strengths of all of the slip systems at a material point are taken to be equal, i.e. we adopt the Taylor hardening assumption. The hardening as a function of accumulated slip

$$\gamma = \int_0^t \sum_{\alpha=1}^{N} \dot{\gamma}^\alpha \, dt' \tag{13}$$

is assumed to follow the macroscopic strain hardening behaviour obtained from a biaxial test by fitting the experimental data to a Voce equation

$$\sigma = 445.21 - 258.0 \exp(-5.1203\varepsilon) \text{ MPa} \tag{14}$$

where a satisfactory fit was obtained beyond $\varepsilon = 0.08$. The fit was adjusted by the average Taylor factor using an approximate value of three to give the slip system resistance to shear, equation (12), as a function of the accumulated shear:

$$\hat{\tau}^\alpha = 148.4 - 86.13 \exp(-1.0768\gamma) \text{ MPa}. \tag{15}$$

When applied in a polycrystal simulation of a tensile test, this treatment of the slip system hardening will approximately reproduce the hardening behaviour that was originally measured. The cubic elastic constants used in the simulation are typical for aluminium: $C_{11} = 108$ GPa, $C_{12} = 62$ GPa and $C_{44} = 28.3$ GPa (Smethells 1983).

2.2. Original specimen and finite-element discretization

The original specimen approximated here by the two-dimensional finite-element simulation was a quasi two dimensional columnar grain polycrystal of high-purity aluminium created by directional solidification (Becker 1998). The material was subsequently annealed to eliminate small grains and irregularities from the grain boundaries. The resulting grain size was of
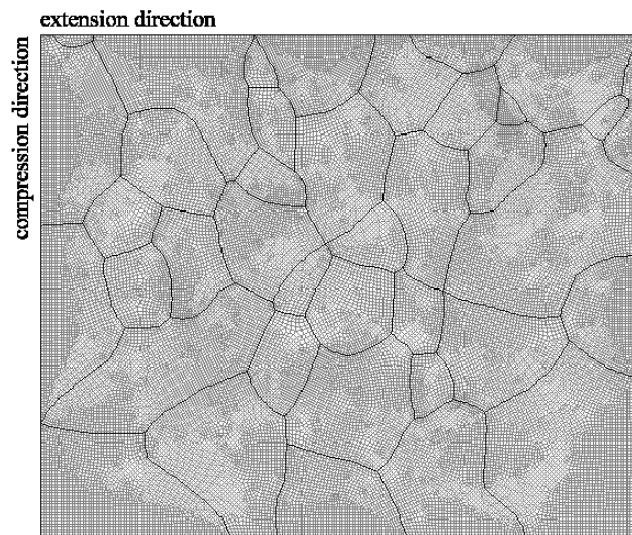
Figure 1. Distribution of the integration point locations in the finite-element mesh before deformation. According to a section of the real specimen, the finite-element sample has a size of 30×25 mm^2. The compression axis is along the 25 mm direction and extension is along the 30 mm direction.

the order of millimetres. A rectangular specimen $30 \times 25 \times 10$ mm^3 was excised for plane strain compression in a channel die. The axis of the columnar grains was aligned with the 10 mm direction of the sample. This was also the constraint direction for the channel die experiments. The compression axis was along the 25 mm direction and extension was along the 30 mm direction. The specimen was etched to reveal the grain structure. The crystal orientations of the 39 grains were determined using the electron backscatter technique in a scanning electron microscope. Both the grain structure and the crystallographic orientations taken from longitudinal sections were provided as input to the two-dimensional finite-element analyses.

Because a fine spatial discretization is desired for coupling the deformation results with the recrystallization model, a two-dimensional finite-element model was constructed. The finite-element mesh was created using the package Maze (1993). This mesh generator uses a paving algorithm in two dimensions to construct a mesh within each individual grain contour. The nodal locations are the same for elements on both sides of a grain boundary. The deformation was modelled as being continuous across grain boundaries. Grain boundary sliding and separation are not permitted. The mesh (figure 1) used 36 977 quadrilateral elements in the model plane.

3. The probabilistic cellular automaton

3.1. Fundamentals

The recrystallization model is designed as a cellular automaton with a probabilistic switching rule (Raabe 1998a,b, 1999). Independent variables are time t and space $x = (x_1, x_2, x_3)$. Space is discretized into an array of equally shaped quadratic cells. Each cell is characterized in terms of the dependent variables. These are scalar (mechanical, electromagnetic) and configurational (interfacial) contributions to the driving force and the crystal orientation $g = g(\varphi_1, \phi, \varphi_2)$,

where g is the rotation matrix and φ_1, ϕ, φ_2 the Euler angles. The driving force is the negative change in Gibbs enthalpy G_t per transformed cell. The starting data, i.e. the crystal orientation map and the spatial distribution of the driving force, must be provided by experiment, i.e. orientation imaging microscopy via electron backscatter diffraction or by simulation, for example a crystal plasticity finite-element simulation as in this study. Grains or subgrains are mapped as regions of identical crystal orientation, but the driving force may vary inside these areas.

The kinetics of the automaton result from changes in the state of the cells, which are hereafter referred to as cell switches. They occur in accord with a switching rule, which determines the individual switching probability of each cell as a function of its previous state and the state of its neighbouring cells. The switching rule used in the simulations discussed below is designed for the simulation of primary static recrystallization. It reflects that the state of a nonrecrystallized cell belonging to a deformed grain may change due to the expansion of a recrystallizing neighbour grain, which grows according to the local driving force and boundary mobility. If such an expanding grain sweeps a nonrecrystallized cell the stored dislocation energy of that cell drops to zero and a new orientation is assigned to it, namely that of the growing neighbour grain.

To put this formally, the switching rule is cast in the form of a probabilistic analogue of the linearized symmetric rate equation of Turnbull (1951), which describes grain boundary motion in terms of isotropic single-atom diffusion processes perpendicular through a homogeneous planar grain boundary segment under the influence of a decrease in Gibbs energy:

$$\dot{x} = n\nu_D\lambda_{gb}c\left\{\exp\left(-\frac{\Delta G + \Delta G_t/2}{k_B T}\right) - \exp\left(-\frac{\Delta G - \Delta G_t/2}{k_B T}\right)\right\} \qquad (16)$$

where $\dot{x}$ is the grain boundary velocity, ν_D the Debye frequency, λ_{gb} is the jump width through the boundary, c is the intrinsic concentration of grain boundary vacancies or shuffle sources, n is the normal of the grain boundary segment, ΔG is the Gibbs enthalpy of motion through in the interface, ΔG_t is the Gibbs enthalpy associated with the transformation, k_B is the Boltzmann constant, and T is the absolute temperature. Replacing the jump width by the burgers vector and the Gibbs enthalpy terms by the total entropy, ΔS, and total enthalpy, ΔH, leads to a linearized form of equation (16):

$$\dot{x} \approx n\nu_D b\exp\left(-\frac{\Delta S}{k_B}\right)\left(\frac{pV}{k_B T}\right)\exp\left(-\frac{\Delta H}{k_B T}\right) \qquad (17)$$

where p is the driving force and V is the atomic volume which is of the order of b^3, where b is the magnitude of the Burgers vector. Summarizing these terms reproduces Turnbull's expression

$$\dot{x} = nmp = nm_0\exp\left(-\frac{Q_{gb}}{k_B T}\right)p \qquad (18)$$

where m is the mobility. Equations (16)–(18) provide a well known kinetic picture of grain boundary segment motion, where the atomistic processes† are statistically described in terms of the pre-exponential factor of the mobility $m_0 = m_0(\Delta g, n)$ and the activation energy of grain boundary mobility $Q_{gb} = Q_{gb}(\Delta g, n)$. Both quantities may depend strongly on the misorientation Δg across the boundary, the grain boundary normal n, and the impurity content (Gottstein *et al* 1997, 1998, Doherty *et al* 1997, Molodov *et al* 1998).

---

† It must be emphasized in this context that thermal fluctuations, i.e. random forward and backward jumps of the atoms through the grain boundary are already included in equation (16). It is not required to consider any additional form of thermal fluctuation.

For dealing with competing switches affecting the same cell, the deterministic rate equation, equation (18), can be replaced by a probabilistic analogue that allows one to calculate switching probabilities. First, equation (18) is separated into a deterministic part, $\dot{x}_0$, which depends weakly on temperature, and a probabilistic part, w, which depends strongly on temperature:

$$\dot{x} = \dot{x}_0 w = n \frac{k_B T m_0}{V} \frac{pV}{k_B T} \exp\left(-\frac{Q_{gb}}{k_B T}\right) \qquad \text{with}$$

$$\dot{x}_0 = n \frac{k_B T m_0}{V} \qquad w = \frac{pV}{k_B T} \exp\left(-\frac{Q_{gb}}{k_B T}\right). \tag{19}$$

The probability factor w represents the product of the linearized part $pV/(k_B T)$ and the nonlinearized part $\exp(-Q_{gb}/(k_B T))$ of the original Boltzmann terms. According to equation (19), nonvanishing switching probabilities occur for cells which reveal neighbours with a different orientation and a driving force which points in their direction. The automaton considers the first-, second- ($2D$), and third- ($3D$) neighbour shells for the calculation of the total driving force acting on a cell. The local value of the switching probability depends on the crystallographic character of the boundary segment between such unlike cells.

3.2. The scaled and normalized switching probability

The cellular automaton is usually applied to starting data that have a spatial resolution far above the atomic scale. This means that the automaton grid may have some mesh size $\lambda_m \gg b$. If a moving boundary segment sweeps a cell, the grain thus grows (or shrinks) by λ_m^3 rather than b^3. Since the net velocity of a boundary segment must be independent of the imposed value of λ_m, an increase of the jump width must lead to a corresponding decrease of the grid attack frequency, i.e. to an increase of the characteristic time step, and *vice versa*. For obtaining a scale-independent grain boundary velocity, the grid frequency must be chosen in a way to ensure that the attempted switch of a cell of length λ_m occurs with a frequency much below the atomic attack frequency that attempts to switch a cell of length b. Mapping equation (19) on a grid which is prescribed by an external scaling length λ_m leads to the equation

$$\dot{x} = \dot{x}_0 w = n(\lambda_m \nu) w \qquad \text{with} \qquad \nu = \frac{k_B T m_0}{V \lambda_m} \tag{20}$$

where ν is the eigenfrequency of the chosen mesh characterized by the scaling length λ_m.

The eigenfrequency given by equation (20) represents the attack frequency for *one* particular grain boundary with constant mobility. In order to use a whole *spectrum* of mobilities and driving forces in one simulation it is necessary to normalize equation (20) by a common grid attack frequency ν_0 rendering it into

$$\dot{x} = \dot{x}_0 w = n \lambda_m \nu_0 \left(\frac{\nu}{\nu_0}\right) w = \hat{\dot{x}}_0 \left(\frac{\nu}{\nu_0}\right) w = \hat{\dot{x}}_0 \hat{w} \tag{21}$$

where the normalized switching probability amounts to

$$\hat{w} = \left(\frac{\nu}{\nu_0}\right) \frac{pV}{k_B T} \exp\left(-\frac{Q_{gb}}{k_B T}\right) = \frac{m_0 p}{\lambda_m \nu_0} \exp\left(-\frac{Q_{gb}}{k_B T}\right). \tag{22}$$

The value of the normalization or grid attack frequency ν_0 can be identified by using the physically plausible assumption that the maximum occurring switching probability cannot be larger than one:

$$\hat{w}^{max} = \frac{m_0^{max} p^{max}}{\lambda_m \nu_0^{min}} \exp\left(-\frac{Q_{gb}^{min}}{k_B T}\right) \leqslant 1 \tag{23}$$

where $m_0^{\max}$ is the maximum occurring pre-exponential factor of the mobility, $p^{\max}$ is the maximum possible driving force, $\nu_0^{\min}$ is the minimum allowed grid attack frequency, and $Q_{\text{gb}}^{\min}$ is the minimum occurring activation energy. With $\hat{w}^{\max} = 1$ in equation (23), one obtains the normalization frequency as a function of the upper bound input data:

$$\nu_0^{\min} = \frac{m_0^{\max} p^{\max}}{\lambda_{\text{m}}} \exp\left(- \frac{Q_{\text{gb}}^{\min}}{k_{\text{B}} T} \right). \tag{24}$$

This frequency and the local values of the mobility and the driving force change equation (22) into

$$\hat{w}^{\text{local}} = \frac{m_0^{\text{local}} p^{\text{local}}}{\lambda_m \nu_0^{\min}} \exp\left(- \frac{Q_{\text{gb}}^{\text{local}}}{k_{\text{B}} T} \right) = \left(\frac{m_0^{\text{local}}}{m_0^{\max}} \right) \left(\frac{p^{\text{local}}}{p^{\max}} \right) \exp\left(- \frac{(Q_{\text{gb}}^{\text{local}} - Q_{\text{gb}}^{\min})}{k_{\text{B}} T} \right)$$

$$= \left(\frac{m^{\text{local}} p^{\text{local}}}{m^{\max} p^{\max}} \right). \tag{25}$$

This expression is the central switching equation of the algorithm. It reveals that the local switching probability can be quantified by the ratio of the local and the maximum mobility $m^{\text{local}}/m^{\max}$, which is a function of the grain boundary character and by the ratio of the local and the maximum driving pressure $p^{\text{local}}/p^{\max}$. The probability of the fastest occurring boundary segment (characterized by $m_0^{\text{local}} = m_0^{\max}$, $p^{\text{local}} = p^{\max}$, $Q_{\text{gb}}^{\text{local}} = Q_{\text{gb}}^{\min}$) to realize a cell switch is equal to one. Equation (25) shows that the mesh size does not influence the switching probability but only the time step elapsing during an attempted switch. The characteristic time constant of the simulation Δt is $1/\nu_0^{\min}$, equation (24).

The switching probability expressed by equation (25) can also be formulated in terms of the local time $t = \lambda_{\text{m}}/\dot{x}$ required by a grain boundary with velocity $\dot{x}$ to cross the automaton cell of size λ_{m} (Gottstein 1999):

$$\hat{w}^{\text{local}} = \left(\frac{m^{\text{local}} p^{\text{local}}}{m^{\max} p^{\max}} \right) = \left(\frac{\dot{x}^{\text{local}}}{\dot{x}^{\max}} \right) = \left(\frac{t^{\max}}{t^{\text{local}}} \right). \tag{26}$$

Therefore, the local switching probability can also be regarded as the ratio of the distances that were swept by the local grain boundary and the grain boundary with maximum velocity, or as the number of time steps the local grain boundary needs to wait before crossing the encountered cell. This reformulates the same underlying problem, namely that boundaries with different mobilities and driving forces cannot equally switch the state of the automaton in a given common time step.

There are two ways to cope with the problem. Either the time step is chosen such that the boundary with minimum probability crosses the cell, then the automaton will always switch state and boundaries with larger velocities will effect neighbouring cells. This is the approach Reher (1998) and Marx *et al* (1995, 1997, 1998) have chosen in their modified automaton. The alternative way is to clock the time step such as to have the boundary with the maximum velocity to cross the cell during one time step. In such a case, more slowly moving boundaries will not switch the cell and one would have to install a counter in the cell to account for that delay. The approach used in this paper principally pursues the latter method and solves it by using a stochastic decision rather than a counter to account for the insufficient sweep of the boundary through the cell. Stochastic Markov-type sampling is equivalent to installing a counter, since the probability to switch the automaton is proportional to the velocity ratio given by equations (25) and (26), provided the chosen random number generator is truly stochastic.

3.3. The switching decision

Equations (25) and (26) allow one to calculate the switching *probability* of a cell as a function of its previous state and the state of the neighbouring cells. The actual *decision* about a switching event for each cell is made by a Monte Carlo step. The use of random sampling ensures that all cells are switched according to their proper statistical weight, i.e. according to the local driving force and mobility between cells. The simulation proceeds by calculating the individual local switching probabilities $\hat{w}^{\text{local}}$ according to equation (25) and evaluating them using a nonMetropolis Monte Carlo algorithm. This means that for each cell the calculated switching probability is compared to a randomly generated number r which lies between zero and one. The switch is accepted if the random number is equal or smaller than the calculated switching probability. Otherwise the switch is rejected:

$$\text{random number } r \text{ between zero and one} \begin{cases} \text{accept switch} & \text{if } r \leqslant \left(\frac{m^{\text{local}} p^{\text{local}}}{m^{\text{max}} p^{\text{max}}} \right) \\ \text{reject switch} & \text{if } r > \left(\frac{m^{\text{local}} p^{\text{local}}}{m^{\text{max}} p^{\text{max}}} \right) \end{cases}. \quad (27)$$

Except for the probabilistic evaluation of the analytically calculated transformation probabilities, the approach is entirely deterministic. Thermal fluctuations other than included through equation (16) are not permitted. The use of realistic or even experimental input data for the grain boundaries (e.g. Gottstein *et al* 1997, 1998, Gottstein and Shvindlerman 1999, Molodov *et al* 1998) enables one to make predictions on a real time and space scale. The switching rule is scalable to any mesh size and to any spectrum of boundary mobility and driving force data. The state update of all cells is made in synchrony.

4. Coupling the crystal plasticity finite-element model with the probabilistic cellular automaton

4.1. Basic considerations about coupling

The coupling between the crystal plasticity finite-element model and the probabilistic cellular automaton was realized in four steps. First, the state variables of the finite-element plasticity model (crystal orientation and accumulated shear) were extracted and translated into state variables of the cellular automaton model (crystal orientation and dislocation density). Second, the integration point locations from the distorted finite-element mesh were mapped on the quadratic mesh of the automaton. Third, the resulting cell size, the maximum occurring driving force, and the maximum occurring grain boundary mobility were extracted from the mapped data for the determination of the length scale λ_{m}, the time step $\Delta t = 1/\nu_0^{\text{min}}$ which elapses during the synchronous state update, equation (24), and the local switching probabilities $\hat{w}^{\text{local}}$, equation (25). Fourth, an appropriate nucleation criterion was defined in order to determine under which kinetic and thermodynamic conditions recrystallization started and which crystal orientations the switched nucleation cells assumed.

4.2. Selection of state variables

The first step in coupling the two methods consists in extracting or, respectively, translating appropriate state variables of the crystal plasticity finite-element model into state variables of the cellular automaton model. The state variables required in the recrystallization model are the crystal orientation and some measure for the stored elastic energy, e.g. the stored dislocation
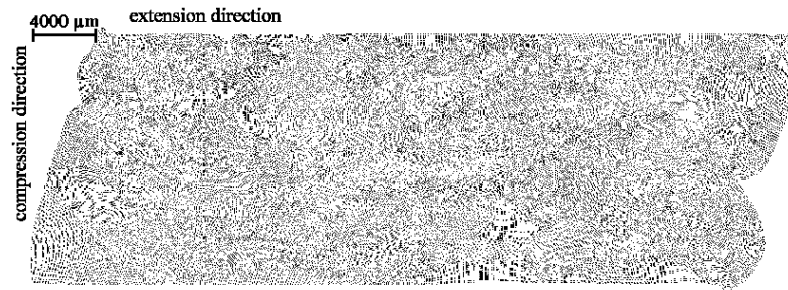
Figure 2. Distribution of the integration point locations in the finite-element mesh at a logarithmic strain of $\varepsilon = -0.434$.

density†. The state variables are given at the spatial coordinates of the integration points of the finite-element mesh.

The crystal orientations at these coordinates, i.e. the microtexture, was not discretized but directly used as calculated by the crystal plasticity finite-element method. Earlier calculations (Raabe 1998a,b) used a discretization method where each orientation is represented by the closest texture component from a set of discrete crystal orientations. The set contained 936 texture components which were equally distributed in orientation space. The use of a continuous instead of a discrete orientation space enhances the calculation speed. However, the required computer memory is enhanced as well.

The second state variable, i.e. the stored dislocation density was linearly related to the value of the accumulated slip known for each nodal point in the finite-element model. It should be noted at this point that recent crystal plasticity polycrystal simulations have not only predicted stored elastic energy arising from the accumulated shear (translated here into some stored dislocation density), but also some local residual elastic stresses which are orientation dependent, although these are not proportional to the shear accumulated during plastic deformation (Dawson *et al* 1999). At large plastic strains this additional elastic incompatibility pressure might not be significant, since the driving forces stemming from stored dislocations typically exceed those stemming from residual elastic stresses by at least an order of magnitude. However, at small strains it could be important to add these elastic stresses to the driving pressure.

4.3. Mapping procedure

The mesh of the finite-element model was aligned with each individual grain contour (figure 1). Since the grains revealed different kinematics and different strain hardening behaviours during deformation the mesh gradually became even more distorted with increasing strain. Figure 2 shows the distribution of the integration points at a logarithmic strain of $\varepsilon = 0.434$. The state variables given at these points had to be mapped on the regular cellular automaton mesh that consisted of quadratic cells.

Spatial compatibility between both types of models can, in principle, be attained by either directly interpolating the finite-element data on a quadratic cellular automaton mesh or by choosing an appropriate mapping procedure. The method we used is a Wigner–Seitz

† Recrystallization models working on a more microscopic scale would also aim at the incorporation of the dislocation cell structure (e.g. Humphreys 1992, 1997, Doherty *et al* 1997). Progress in recrystallization and recovery could then be described by discontinuous (recrystallization) and continuous (recovery) subgrain coarsening. The approach presented here works on a somewhat larger scale where dislocation cell coarsening is not explicitly considered.

cellular automaton   + finite element
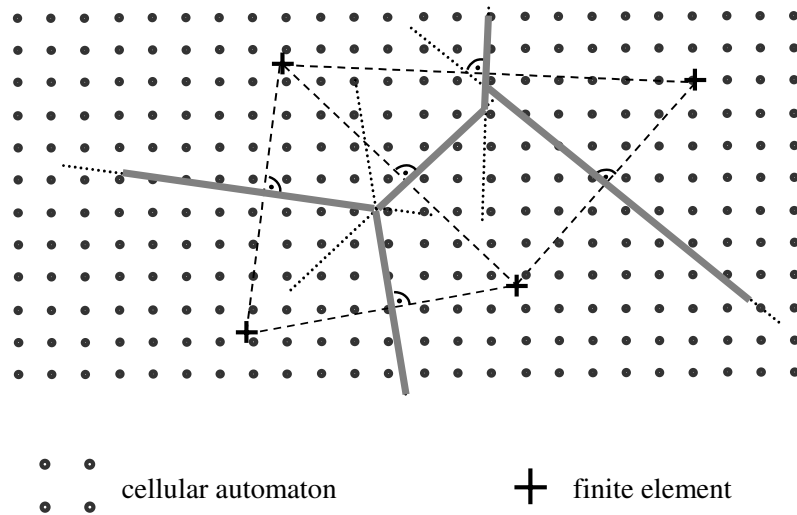
Figure 3. Schematic description of the Wigner–Seitz mapping algorithm. It consists of two steps. First, a fine quadratic grid (circles) is superimposed on the finite-element mesh (crosses). Second, values of the state variables at each of the integration points are assigned to the new grid points that fall within the Wigner–Seitz cell corresponding to that integration point. The Wigner–Seitz cells of the finite-element mesh are constructed from cell walls, which are the perpendicular bisecting planes of all lines connecting neighbouring integration points, i.e. the integration points are in the centres of the Wigner–Seitz cells.

type of mapping algorithm (Raabe 1999). It consisted of two steps. In the first step, a fine quadratic automaton grid was superimposed on the distorted finite-element mesh. The spacing of the points in the new grid was smaller than the spacing of the closest neighbour points in the finite-element mesh. The absolute value of the cell size of the superimposed quadratic cellular automaton mesh was thus determined by the size of the simulated specimen (see section 2.2). It amounted to $\lambda_m = 61.9$ μm. While the original finite-element mesh consisted of 36 977 quadrilateral elements, the cellular automaton mesh consisted of 217 600 cells. In the second step, values of the state variables at each of the integration points were assigned to the new grid points that fell within the Wigner–Seitz cell corresponding to that integration point. The Wigner–Seitz cells of the finite-element mesh were constructed from cell walls, which were the perpendicular bisecting planes of all lines connecting neighbouring integration points (figure 3), i.e. the integration points were in the centres of the Wigner–Seitz cells.

The Wigner–Seitz procedure requires that the cellular automaton grid is finer than the finite-element mesh, i.e. this mapping method produces clusters of cellular automaton sites with identical state variable properties surrounding each finite-element interpolation point. In the model these clusters correspond to regions of the same crystallographic orientation with a uniform nonzero dislocation density. The size of these cellular automaton clusters depends on the ratio between the average finite element point spacing and the cellular automaton site spacing. Since, at a later stage of the simulation (section 4.5), a nucleation criterion must be defined as a function of the local misorientation between neighbouring automaton cells, and since this criterion is only satisfied at the boundaries of the cellular automaton clusters, it is conceivable that the Wigner–Seitz approach might introduce a dependence on the finite-element mesh size.
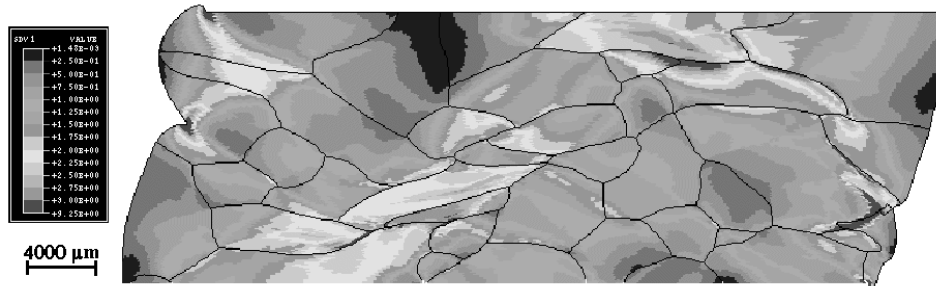
Figure 4. Distribution of the accumulated crystallographic shear strain in the finite-element sample at a logarithmic deformation of $\varepsilon = -0.434$.

4.4. Scaling procedure

The maximum driving force in the region arising from the stored dislocation density amounted to about 1 MPa. The temperature dependence of the shear modulus and of the Burgers vector was considered in the calculation of the driving force. The grain boundary mobility in the region was characterized by an activation energy of the grain boundary mobility of 1.46 eV and a pre-exponential factor of the grain boundary mobility of $m_0 = 8.3 \times 10^{-3} \text{ m}^3 \text{ N}^{-1} \text{ s}^{-1}$. Together with the scaling length $\lambda_m = 61.9 \ \mu$m we used these data for the calculation of the time step $\Delta t = 1/\nu_0^{\min}$, equation (24), and of the local switching probabilities $\hat{w}^{\text{local}}$, equation (25).

4.5. Nucleation criterion for recrystallization

The nucleation process during primary static recrystallization has been explained for pure aluminium in terms of discontinuous subgrain growth (Humphreys 1992, 1997, Doherty *et al* 1997). According to this model nucleation takes place in areas which reveal high misorientations among neighbouring subgrains and a high driving force for curvature-driven subgrain coarsening. The present simulation approach works above the subgrain scale, i.e. it does not explicitly describe cell walls and subgrain coarsening phenomena. Instead, we incorporated nucleation on a more phenomenological basis using the kinetic and thermodynamic instability criteria known from classical recrystallization theory (Himmel 1963, Haessner 1978, Gottstein 1984, Humphreys and Hatherly 1995). The kinetic instability criterion means that a successful nucleation process leads to the formation of a mobile, large-angle grain boundary. The thermodynamic instability criterion means that the stored energy changes across the newly formed large-angle grain boundary providing a net driving force. Nucleation in this simulation is performed in accord with these two aspects, i.e. potential nucleation sites must fulfil both the kinetic and the thermodynamic instability criterion. In the simulations two phenomenological nucleation models were implemented based on these instability criteria.

The first nucleation model is a variant of the subgrain coalescence model and is capable of creating new orientations. At the beginning of the simulation the kinetic conditions for nucleation were checked by calculating the misorientations among all neighbouring cells. If a pair of cells revealed a misorientation above 15°, the thermodynamic criterion, i.e. the local value of the dislocation density was also checked. If the dislocation density was larger than some critical value of its maximum value in the sample (we checked 10%, 30%, 50%, 70%, 80% and 90%), the two cells were recrystallized, i.e. a new orientation midway between the two

(*a*)

(*b*)

(*c*)

(*d*)
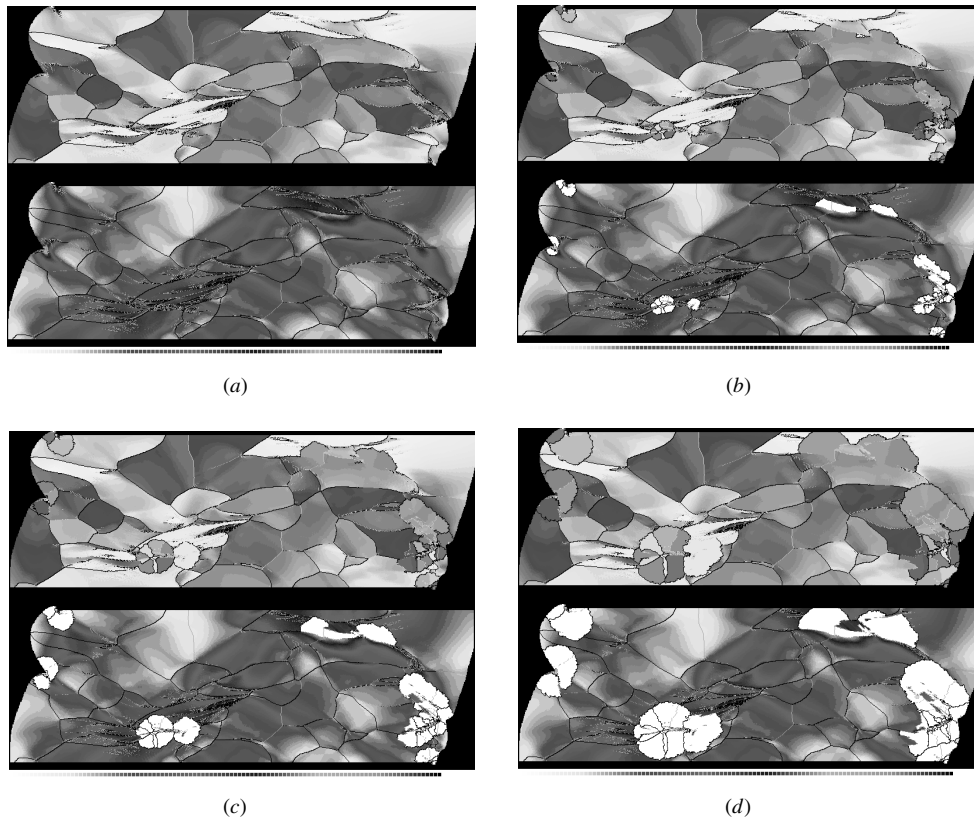
Figure 5. 2D simulations of primary static recrystallization in a deformed aluminium polycrystal on the basis of crystal plasticity finite-element data. The figure shows the change both in microtexture (upper images) and in dislocation density (lower images), which was derived from the value of the accumulated crystallographic shear, as a function of the annealing time during isothermal recrystallization. The white areas in the lower images indicate a stored dislocation density of zero, i.e. they are recrystallized. The black lines in both figures indicate misorientations above 15° and the thin grey lines indicate misorientations between 5° and 15°, irrespective of the rotation axis. The orientation image given in the upper figures represents different crystal orientations by different grey levels. The simulation parameters are: annealing temperature, 800 K; site-saturated nucleation conditions; kinetic instability criterion, misorientation above 15°; thermodynamic instability criterion, dislocation density larger than 70% of the maximum occurring value; maximum occurring driving force, 1 MPa; activation energy of the grain boundary mobility, 1.46 eV; pre-exponential factor of the grain boundary mobility, $m_0 = 8.3 \times 10^{-3}$ m^3 N^{-1} s^{-1} and mesh size of the cellular automaton grid (scaling length), $\lambda_m = 61.9$ μm. The images show a crystal in the following states of recrystallization: (*a*) 0%, (*b*) 3%, (*c*) 13%, (*d*) 22%, (*e*) 32%, (*f*) 48%, (*g*) 82% and (*h*) 93% recrystallized.

original orientations was created and a dislocation density of zero was assigned to them. The generation of the new orientation was based on the idealized picture of subgrain coalescence (Hu 1963). If the two recrystallized cells had a misorientation above 15° with respect to the nonrecrystallized neighbour cells they could grow into the surrounding matrix.

The second nucleation model is even simpler and does not create new orientations. At the beginning of the simulation, the thermodynamic criterion, i.e. the local value of the dislocation density, was first checked for all grid points. If the dislocation density was larger than some critical value of its maximum value in the sample (we checked 10%, 30%, 50%, 70%, 80%
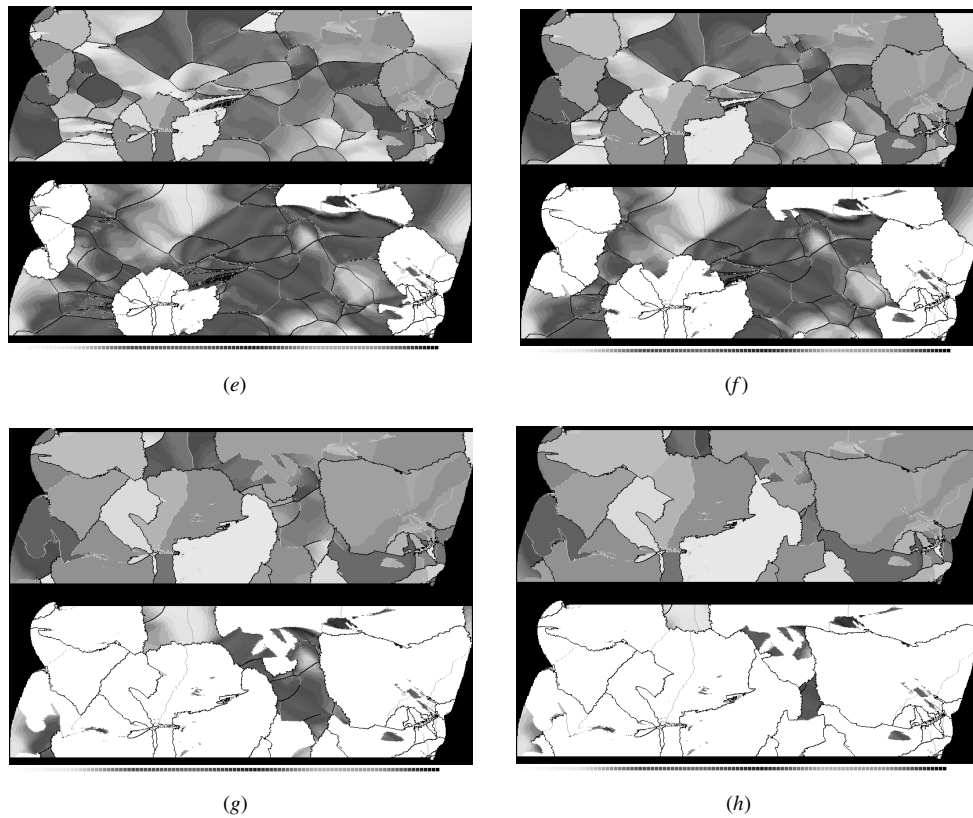
(*e*)

(*f*)

(*g*)

(*h*)

Figure 5. (Continued)

and 90%), the cell was spontaneously recrystallized without any orientation change, i.e. a dislocation density of zero was assigned to it and the original crystal orientation was preserved. In the next step the ordinary growth algorithm was started according to equations (25)–(27), i.e. the kinetic conditions for nucleation were checked by calculating the misorientations among all spontaneously recrystallized cells (preserving their original crystal orientation) and their immediate neighbourhood considering the first-, the second-, and the third-neighbour shells. If any such pair of cells revealed a misorientation above 15°, the cell flip of the unrecrystallized cell was calculated according to equations (25)–(27). In case of a successful cell flip, the orientation of the first recrystallized neighbour cell was assigned to the flipped cell. All simulation results presented hereafter used the second nucleation model.

5. Simulation of primary static recrystallization

Figure 4 shows the starting conditions prior to the simulated annealing treatment, i.e. the distribution of the accumulated crystallographic shear in the sample after a total logarithmic strain of $\varepsilon = -0.434$. The distribution of the integration points of the finite-element mesh was shown in figure 2. Figure 4 reveals three major areas with large values of the accumulated shear (bright areas). These areas can be referred to as deformation bands.

    Figure 5 shows the change both in microtexture and in dislocation density, which was assumed to be proportional to the accumulated crystallographic shear, as a function of the
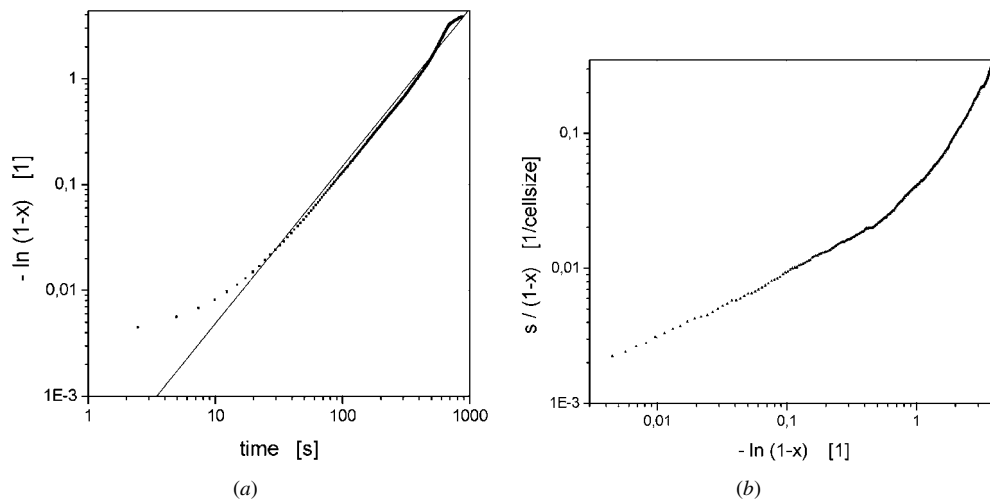
Figure 6. Simulated recrystallized volume fraction ((a) Avrami diagram) and interface fraction ((b) Cahn–Hagel diagram) as functions of the annealing time. The temperature was 800 K.

annealing time during recrystallization. The annealing temperature was 800 K. The simulation assumed site-saturated nucleation conditions using the second nucleation criterion described in the preceding section, i.e. potential nuclei were spontaneously formed at $t = 0$ s in cells with a dislocation density larger than 70% of the maximum value in the sample. These potential nuclei then grew or remained unchanged in accord with equations (25)–(27).

The upper images in figure 5 show the orientation images where each grey level represents a specific crystal orientation. The grey level is calculated as the magnitude of the Rodriguez orientation vector. The cube component serves as a reference orientation. The lower images in figure 5 show the stored dislocation densities. The white areas are recrystallized, i.e. the stored dislocation content of the affected cells was dropped to zero. The black lines in both figures indicate misorientations above 15° irrespective of the rotation axis. The thin grey lines in both figures indicate misorientations above 5° and below 15° irrespective of the rotation axis.

The incipient stages of recrystallization (figures 5(a)–(c)) reveal that nucleation is concentrated in areas with large accumulated local shear strains and lattice curvatures (figure 4). This means that the spatial distribution of the nuclei is very inhomogeneous. The deformation bands with high localized stored energy and lattice curvature produce clusters of similarly oriented nuclei. Less deformed areas between the bands show a negligible density of nuclei. The following stages of recrystallization (figures 5(d)–(f)) reveal that the nuclei do not grow freely into the surrounding deformed material as described by Avrami–Johnson–Mehl theory, but impinge upon each other and thus compete, already, at a very early stage of the transformation. The late stages of recrystallization show an incomplete and spatially heterogeneous transformation of the deformed material (figures 5(g) and (h)).

The observed deviation from Avrami–Johnson–Mehl-type growth, i.e. the early impingement is reflected by the kinetic behaviour which differs from the classical sigmoidal kinetics observed under homogeneous nucleation conditions (figure 6). The kinetics simulated on the basis of the finite-element data in conjunction with the chosen nucleation model reveal an Avrami exponent of about 1.4, which is for below the theoretical value for site-saturated
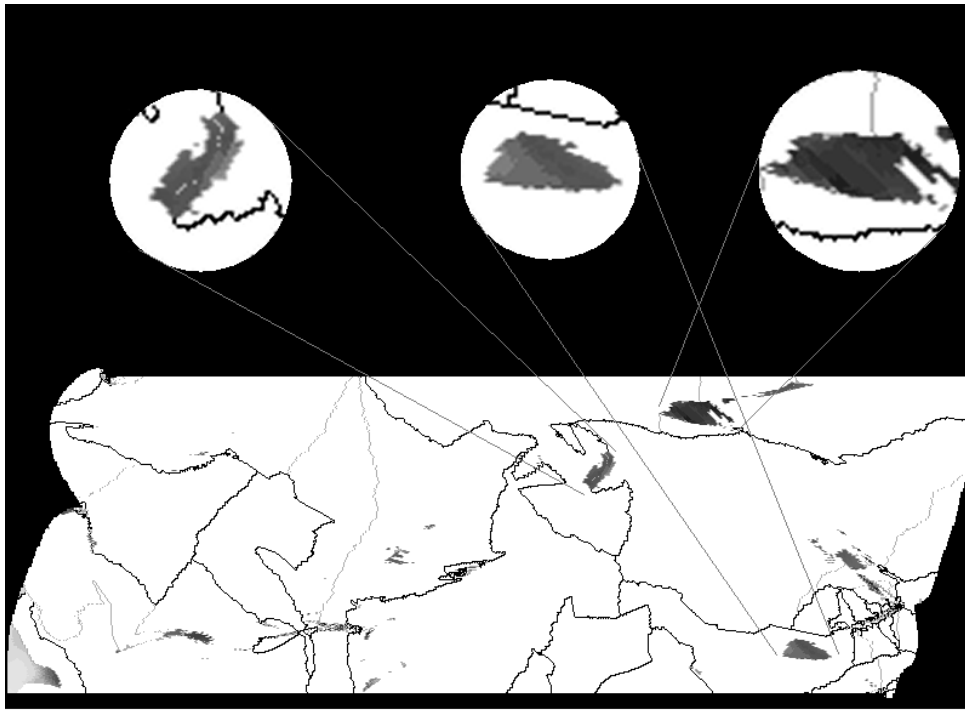
Figure 7. Magnification of three selected areas where moving large-angle grain boundaries did not sweep the deformed material. This pronounced recovery is due to insufficient misorientations between the deformed and the recrystallized areas entailing a drop in grain boundary mobility (orientation pinning).

nucleation conditions in two dimensions of two (figure 6(*a*)). Figure 6(*b*) shows the corresponding Cahn–Hagel plot. A more systematic analysis of such nucleation behaviour, which is characterized by an early growth competition, might help to identify approaches for the optimization and even tailoring of recrystallization kinetics, texture, and grain size.

Another interesting result of the simulation is the partial recovery of deformed material. Figure 7 shows three selected areas where moving large angle-grain boundaries did not sweep the deformed material. An analysis of the state variable values at these coordinates and of the grain boundaries involved substantiates that not insufficient driving forces, but insufficient misorientations between the deformed and the recrystallized areas—entailing a drop in grain boundary mobility—were responsible for this effect. Previous authors referred to this mechanisms as orientation pinning (Juul Jensen 1997).

Figure 8 shows the crystallographic textures of the microstructures presented in figure 5. The orientation distribution functions were calculated by replacing each single orientation by a Gauss-type scattering functions using a scatter width of $3°$. The textures are given in Euler space where each coordinate φ_1, ϕ, φ_2 represents a certain crystal orientation. In order to emphasize the main texture components in Euler space, only areas with an orientation density above random ($f(g) = 1$) are plotted. The initial texture is characterized by a number of isolated components, some partial texture fibres, and some smeared-out components. During the annealing treatment most of the scattered components vanish and the main texture components are shifted.

(*a*)   (*b*)
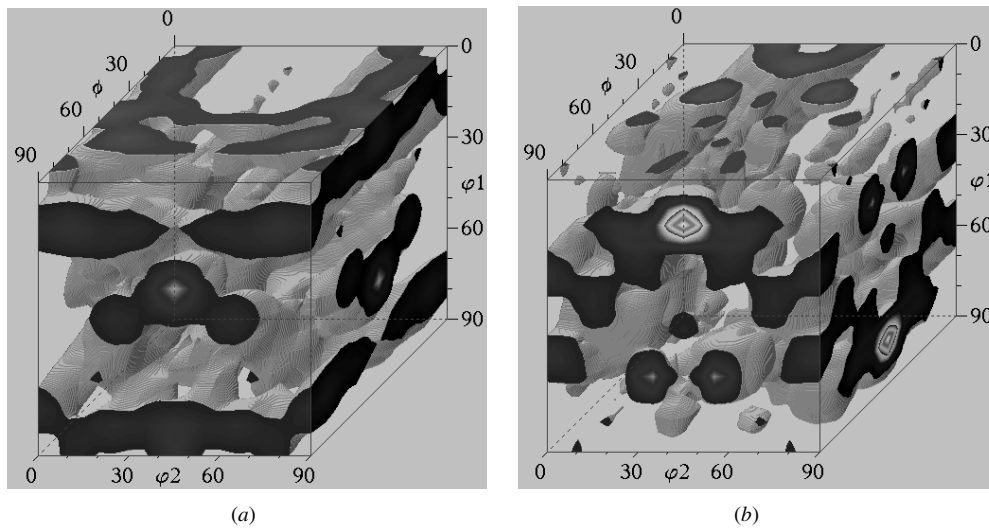
Figure 8. Starting (*a*) and end (*b*) texture of the microstructures shown in figure 5. The orientation distribution functions were calculated by using Gauss-type scattering functions with a scatter width of 3°. The textures are given in Euler space where each coordinate $\varphi_1, \phi, \varphi_2$ represents a certain crystal orientation. In order to emphasize the main texture components, the graphs show only areas in Euler space with an orientation density above random ($f(g) = 1$).

6. Conclusions

We presented an approach for simulating recrystallization by coupling a viscoplastic crystal plasticity finite-element model with a cellular automaton. The coupling between both models consisted of: extracting and translating the microtexture and stored energy data predicted by the finite-element simulation into the cellular automaton model; mapping these data on the quadratic cellular automaton mesh; scaling the cellular automaton in terms of the derived cell size, maximum driving force, and maximum grain boundary mobility occurring in the region; and establishing an adequate nucleation criterion, which makes use of these data. The coupling method was used to simulate the formation of texture and microstructure in a deformed high-purity aluminium polycrystal during static primary recrystallization. It was observed that nucleation was concentrated in areas with a large accumulated shear and large lattice curvature. The spatial distribution of the nuclei was very inhomogeneous. Deformation bands with high stored energy and large curvature showed a high density of nuclei, whilst less deformed areas did not produce nuclei. The clustering of nuclei led to a deviation from Avrami–Johnson–Mehl-type kinetics with a 2D Avrami exponent significantly below two. The observed partial recovery of deformed material was explained in terms of insufficient misorientations between some of the deformed and the recrystallized areas, which entailed a local drop in grain boundary mobility. The initial texture after deformation was changed during the recrystallization treatment.

Acknowledgments

References

Abaqus Users' Manual 1994 Hibbitt, Karlsson and Sorensen, Pawtucket, RI

Asaro R J 1983 *Adv. Appl. Mech.* **23** 1–23

Becker R C 1991 *Acta Metall. Mater.* **39** 1211–30

——1998 *Hot Deformation of Aluminum Alloys* vol 2, ed T R Bieler, L A Lalli and S R MacEwen (TMS) pp 255–66

Becker R C, Butler J, Lalli L A and Hu W H 1991 *Metal. Trans.* A **22** 45–58

Becker R C and Panchanadeeswaran S 1995 *Acta Metall. Mater.* **43** 2701–19

Dawson P, Boyce D, MacEwen S and Rogge R *Proc. 12th Int. Conf. on Textures of Materials ICOTOM 12 (Montreal, Canada, August 9–13, 1999)* ed J A Szpunar (Ottawa: NRC Research Press) pp 505–10

Doherty R D, Hughes D A, Humphreys F J, Jonas J J, Juul Jensen D, Kassner M E, King W E, McNelly T R, McQueen H J and Rollett A D 1997 *Mater. Sci. Eng.* A **238** 219–74

Gottstein G 1984 Rekristallisation metallischer Werkstoffe (in German) *DGM Informationsgesellschaft* (Deutsche Gesellschaft für Metallkunde)

——1999 private communication

Gottstein G, Molodov D A and Shvindlerman L S 1998 *Interface Sci.* **6** 7–22

Gottstein G and Shvindlerman L S 1999 *Grain Boundary Migration in Metals—Thermodynamics, Kinetics, Applications* (Boca Raton, FL: CRC Press)

Gottstein G, Shvindlerman L S, Molodov D A and Czubayko U 1997 *Dynamics of Crystal Surfaces and Interfaces* ed P M Duxbury and T J Pence (New York: Plenum) pp 109–123

Haessner F 1978 *Recrystallization of Metallic Materials* (Dr Riederer)

Himmel L 1963 *Recovery and Recrystallization of Metals* (New York: Wiley)

Hu H 1963 *Recovery and Recrystallization of Metals* ed L Himmel (New York: Wiley) p 311

Humphreys J F 1992 *Mater. Sci. Technol.* **8** 135–44

——1997 *Acta Metall.* **45** 4231–53

Humphreys F J and Hatherly M 1995 *Recrystallization and Related Annealing Phenomena* (Oxford: Pergamon)

Juul Jensen D 1997 Orientation aspects of growth during recrystallization *Report* RISØ-R-978 (EN), Materials Research Department, RISØ National Laboratory.

Marx V, Raabe D, Engler O and Gottstein G 1997 *Proc. Symp. Computer Simulation and Modelling in Texture Research (Aachen, October 13–14, 1995)* (*Textures Microstruct.* **28** 211–18 (special edition)) (London: Gordon and Breach) series ed H-J Bunge, volume ed D Raabe and H-J Bunge

Marx V, Raabe D and Gottstein G 1995 Materials: microstructural and crystallographic aspects of recrystallization *Proc. 16th RISØ Int. Symp. on Material Science (RISØ National Laboratory, Roskilde, Denmark)* ed N Hansen, D Juul Jensen, Y L Liu, B Ralph, pp 461–6

Marx V, Reher F R and Gottstein G 1998 *Acta Mater.* **47** 1219–30

Maze Users Manual 1993 *LSTC Report* 1005, Livermore Software Technology Corporation, Livermore, CA

Molodov D A, Czubayko U, Gottstein G and Shvindlerman L S 1998 *Acta Mater.* **46** 553–64

Peirce D, Asaro R J and Needleman A 1983 *Acta Metall.* **31** 1951–76

Raabe D 1998a *Texture and Anisotropy of Polycrystals (Material Science Forum, vol 273–275)* ed R A Schwarzer (Trans Tech) pp 169–74

——1998b *Proc. 3rd Int. Conf. on Grain Growth in Polycrystalline Materials (Carnegie Mellon University, Pittsburgh, 1998)* ed H Weiland, B L Adams and A D Rollett pp 179–85

——1999 *Phil. Mag.* A **79** 2339–58

Reher F 1998 *PhD Dissertation* Rheinisch-Westfälische Technische Hochschule Aachen, Institut für Metallkunde und Metallphysik (in German)

Smelser R E and Becker R C 1989 (*Proc. Abaqus Users' Conf., Strasa, Italy*) (Providence RI: Hibbitt, Karlsson and Sorensen, Inc.) p 207

Smethells Metals Reference Book 1983 6 edn ed E A Brandles (London: Butterworths) p 15

Turnbull D 1951 *Trans. AIME* **191** 661–75